

# Fluorine-Doped Tin Oxide Thin Films with High Surface Conductance and Low Transparency for Boosting Performance in Dye-Sensitized Solar Cell Applications

Roshan Sudarshana Rathnayaka Kananke Udubokke Rathnayakage, Thennakoon Mudiyansele Wijendra Jayalath Bandara,\* Kapila Wijayarathne, Gamaralalage Rajanya Asoka Kumara, Landewatte Ajith de Silva, and Kirthi Tennakone

Cite This: <https://doi.org/10.1021/acsaem.3c00058>

Read Online

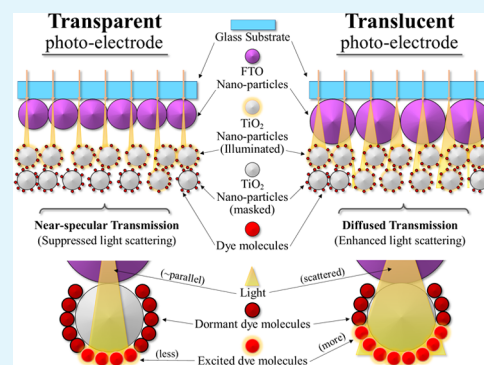
ACCESS |

Metrics & More

Article Recommendations

**ABSTRACT:** Transparent conductive oxide films, like fluorine-doped tin oxide (FTO), are needed for electrochemical devices. FTO films are attractive due to their cost-effectiveness and high-temperature tolerance. Generally, solar cell fabrication requires high transmittance and low-conductivity FTOs. However, achieving both simultaneously poses a fundamental challenge. This study investigates the impact of FTO layer thickness, sheet resistance, transparency, and film morphology on optimizing the performance of dye-sensitized solar cells. To achieve this, a precursor solution containing  $\text{SnCl}_4 \cdot 5\text{H}_2\text{O}$  and  $\text{NH}_4\text{F}$  in isopropanol is sprayed onto a soda-lime glass substrate at  $500\text{ }^\circ\text{C}$  to form FTO films. The film thickness is varied by repeating the spray cycles. By increasing the number of spray cycles, the sheet resistance of the FTO film improves to  $\sim 1.20\ \Omega\ \square^{-1}$  with the expense of transmittance. The achieved very low sheet resistance of  $\sim 1\ \Omega\ \square^{-1}$  ( $\sim 3.54 \times 10^{-4}$ )  $\Omega\ \text{cm}$  resistivity for the FTO film confirms the promise of this sequential spray pyrolysis technique in preparing highly conductive inert electrodes for various applications. Furthermore, DSCs with low transparency and sheet resistance showed higher-energy conversion efficiencies, challenging the current prerequisite of the requirement of high transmittance. The best efficiency (5.14%) is achieved with FTO films having a 34.2% transmittance and a  $3.27\ \Omega\ \square^{-1}$  sheet resistance, outperforming standard FTO films (4.74%) with a  $10\ \Omega\ \square^{-1}$  sheet resistance and an  $\sim 83\%$  transmittance. The results indicate that the transparency of FTO is not a dominant factor and carefully controlled light scattering and electrical properties in translucent FTO films would lead to the realization of dye-sensitized solar cells that deliver superior efficiency.

**KEYWORDS:** dye-sensitized solar cells, fluorine-doped tin oxide, spray pyrolysis, sheet resistance, optical transparency



## INTRODUCTION

Transparent conductive materials (TCMs) are a class of materials having an appreciable optical transmission as well as electrical conductivity. TCMs are generally in the form of thin films.<sup>1</sup> Among various TCM applications, transparent conductive oxide (TCO) substrates are a vital component of many optoelectrical and electrochemical devices. TCOs are usually n- or p-type extrinsic semiconductors with good conductivity and transparency.<sup>2</sup> The doping process increases the conductivity of these oxides, while the higher band gap ( $>3\ \text{eV}$ ) ensures transparency in the visible portion of the spectrum. Thin film solar cells,<sup>3</sup> liquid crystal flat panel displays,<sup>4</sup> OLED displays,<sup>5</sup> and transparent high-mobility thin film transistors (TFTs)<sup>6</sup> are some applications of TCOs. Tin-doped indium oxide (ITO), aluminum-doped zinc oxide (AZO), and fluorine-doped tin oxide (FTO) are some examples of widely used TCOs. ITO is currently the best

TCO available, with the lowest resistivity of  $1\text{--}2 \times 10^{-4}\ \Omega\ \text{cm}$  with an average optical transmittance above 90%.<sup>7,8</sup> However, due to the low availability of indium on Earth, the cost of industrial-scale production is continuously increasing. As a substitute for this, fluorine-doped tin oxide has been developed. FTO has presently become the most popular TCO due to its inexpensiveness, chemical inertness, and higher-temperature tolerance.

Undoped  $\text{SnO}_2$  is a direct band-gap semiconductor with a band gap of about  $3.6\ \text{eV}$ .<sup>9</sup> The crystal structure of the pure

Received: January 15, 2023

Accepted: June 7, 2023

$\text{SnO}_2$  is similar to the rutile structure with a tetragonal unit cell, and it is a native n-type material.<sup>10</sup> n-type characteristic of undoped  $\text{SnO}_2$  originates from the native defects, such as structural imperfection, and unintentional impurities, such as oxygen vacancies and Sn interstitials.<sup>11</sup> Undoped  $\text{SnO}_2$  thin films prepared by advanced sputtering techniques have been reported to have a resistivity of around  $4 \times 10^{-3} \Omega \text{ cm}$ .<sup>12–14</sup> The conductivity of  $\text{SnO}_2$  can further be increased by doping it with elements such as F, Sb, Cl, Br, etc.<sup>15,16</sup> Among these elements, F is the most widely used dopant because the resulting fluorine-doped tin oxide (FTO) coatings are very stable under ambient conditions. For example, they are chemically inert and thermally stable.<sup>17</sup> Due to the similarity of the anionic radius of  $\text{F}^-$  and  $\text{O}^{2-}$ , the lattice distortion induced by  $\text{F}^-$  doping is minimum compared to other cationic dopings (such as Sb, Cl, or Br). Therefore, the FTO has the same crystal structure as pure  $\text{SnO}_2$ . However, the addition of a fluorine dopant increases the band gap of  $\text{SnO}_2$  above 3.6 eV and, by increasing F-doping, the optical band-gap energy in FTO can be increased.<sup>18,19</sup> The widening of the band gap improves the transparency in the ultraviolet (UV) range.

In addition, the literature shows that most of the DSCs fabricated for research purposes utilized commercially available FTO substrates. This restricts the possible variation of some parameters crucial in optimizing cell performance. This work introduces a facile and low-cost method of preparing FTO films and modifying necessary parameters enabling the utilization of tailor-made FTO films in related applications.

The resistivity of FTO is slightly higher than that of AZO and ITO. The lowest values of about  $3\text{--}4 \times 10^{-4} \Omega \text{ cm}$  are being reported along with 75% of optical transmittance in the visible range.<sup>20,21</sup> Compared to  $\text{In}_2\text{O}_3$  and  $\text{ZnO}$ , which require more expensive and sophisticated preparation techniques, FTO can be prepared using facile and inexpensive methods such as spray pyrolysis using cheaper raw materials such as tin chlorides and ammonium fluoride.<sup>19,20,22</sup> Spray pyrolysis is a process in which thin films are deposited by spraying a precursor solution onto a heated surface such that the constituents react on the surface to form the desired chemical compound. The chemical reactants are selected such that the products, other than the desired compound, are volatile at the deposition temperature. The spray pyrolysis method is a relatively cost-effective method used in preparing FTO compared to other methods such as pulsed laser deposition,<sup>23</sup> chemical vapor deposition (CVD),<sup>24</sup> sputtering methods, and DC magnetron sputtering.<sup>25,26</sup>

Several parameters should be carefully controlled during the preparation of the FTO film by spray pyrolysis to optimize optical and electrical properties. Those are tin- and fluorine-dopant concentrations in the precursor solution, the temperature of the glass substrate, gas carrier flow rate, the time between two spray cycles, the distance between the substrate and spray gun, and the type of solvent.

The lowest resistivity, as well as the highest optical transmittance of FTO films obtained via spray pyrolysis, has been recorded when the fluorine compound content is around 15–20 wt % of the tin compound.<sup>27–29</sup> The sheet resistance and optical transmittance of the FTO film reduce with the increase in the film thickness.<sup>30,31</sup> This behavior is a fundamental problem associated with FTO fabrication, which makes the simultaneous optimization of the electrical and optical properties of FTO for optoelectrical applications challenging.

The temperature is a very sensitive regulatory factor in producing thin films from the spray pyrolysis technique since the drying of droplets, decomposition, crystallization, and grain growth strongly depend on the substrate temperature. Suppose the deposition temperature is not higher enough to decompose and volatilize the byproducts, in such a case, the resulting films may have poor adhesivity to the substrate and hence may degrade the quality of the fabricated devices. In accordance with the literature, in order to achieve desirable transparency and conductivity, the pyrolysis temperature is maintained at  $450 \text{ }^\circ\text{C}$  so that the polycrystalline structure of the FTO can develop optimally.<sup>20,32–34</sup>

The carrier gas flow rate and the time between two spray cycles should be controlled to maintain a constant substrate temperature throughout the process while giving enough time for the sintering and crystal growth. The distance between the nozzle and the substrate is also critical because shorter distances result in compact distributions of droplets over the substrate, promoting crystal growth. On the contrary, longer distances may spread the droplets far away, resulting in poor sintering.

Over the last few decades, scientists have conducted extensive research on renewable energy resources such as solar energy, wind energy, ocean energy, geothermal energy, etc., due to high energy demand, limitation of fossil fuel, and global warming. Among these renewable energy sources, solar energy has received more attention due to its cleanness and high energy availability. Several methods are used to convert solar energy to meet human needs, for example, generating electricity by exciting electrons in a solar cell using photons in visible light,<sup>35</sup> producing chemical fuel via artificial photosynthesis,<sup>36</sup> concentrating sunlight to produce heat,<sup>37</sup> etc. Mainly, solar power is gained by converting solar radiation energy into electricity via photovoltaic (PV) devices. Generally, PV technologies are divided into three generations depending on their efficiency and manufacturing cost. The DSCs belong to the third generation of PV technologies, which have low-cost and higher-energy conversion capability.<sup>38</sup> In the present scenario, the research and development of DSCs are ongoing in various branches such as the development of platinum-free counter electrodes,<sup>39,40</sup> nonvolatile electrolytes,<sup>41</sup> high efficient and low-cost photon absorbers,<sup>42</sup> development of photo-electrode by improving the dye adoption, charge transport and injection,<sup>43–45</sup> etc. These studies mainly focused on enhancing the energy conversion efficiency, increase in the durability, stability, and cost-effectiveness of the DSCs. Apart from that, portable, textile, and flexible DSCs are also high-tendency research areas in the present DSC developments.<sup>46</sup>

For solar cell applications, the literature suggests FTO films with an 80% transmittance (glass substrate included) and a sheet resistance of  $10 \Omega \square^{-1}$  as the standard requirement for efficient photovoltaic conversion.<sup>38</sup> Although high transparency and low sheet resistance are usually desired for better performance of DSCs, there is a trade-off between transparency and sheet resistance governed by fundamental system parameters. There are several studies attempting to enhance the efficiency of DSCs by introducing an additional light scattering layer to the photoelectrode fabricated on conventional FTO substrates.<sup>35,43,45,47,48</sup> However, in this study, we wish to present that not just transparent FTO films but also translucent FTO films with carefully controlled light scattering properties can be used to improve the performance of DSCs. In addition, there are several other electrochemical applications

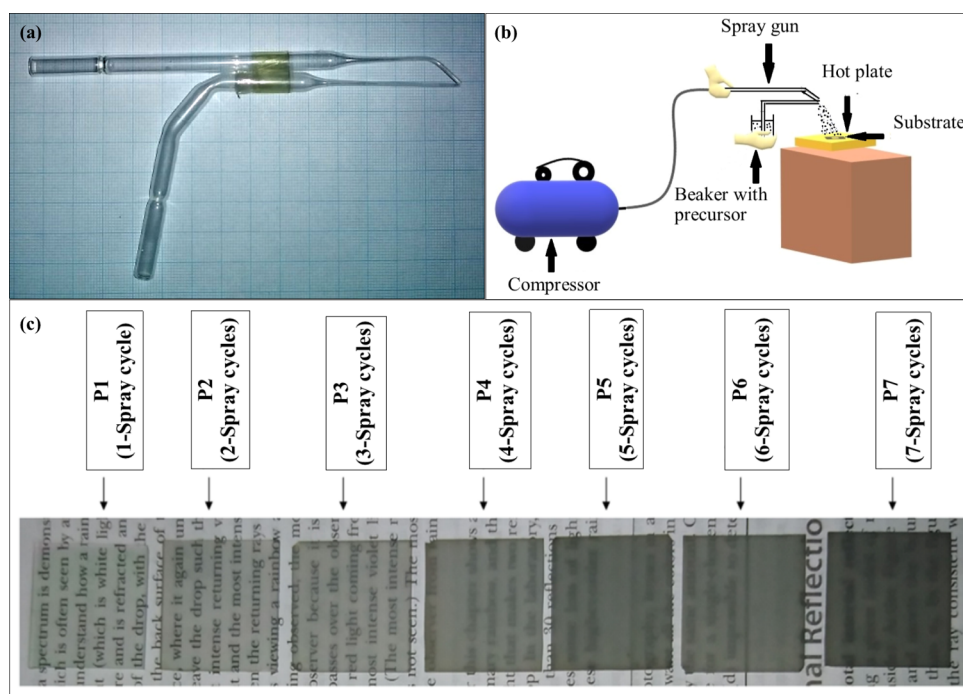


**Figure 1.** (a) Spray gun prepared by using two glass droppers. (b) Schematic diagram of the spray pyrolysis process. (c) Photographs of seven FTO samples prepared by the spray pyrolysis technique.

of highly conducting electrodes since metal electrodes cannot be used with concentrated acids. For such applications, the transparency of the electrode is not essential but requires higher electrical conductivity. In supercapacitors, for instance, the corrosion effect of electrolytes has restricted the use of most highly conducting metals as electrodes.<sup>49–51</sup> As a substitute, supercapacitors use FTO films with high surface conductivity. The ability to alter the surface morphology of FTO thin films confers an added benefit to the electrode material–electrode bonding process. In addition, these FTO coatings with high surface conductance can be used as a conductive protective layer in Li-ion batteries.<sup>52,53</sup> Moreover, FTOs are used as an alternative in electrochemical cells when electrolytes corrode the metal electrodes.<sup>54,55</sup>

In this research, we synthesized and studied the properties of FTO films by varying the deposition time. In this way, we managed to modify the film thickness, sheet resistance, conductivity, transmittance, and film morphology. The electrical, optical, structural, and morphological properties of the synthesized FTO film series were investigated and compared with commercially available FTO reference substrates (CFTO). In order to study the effect of layer deposition parameters on DSC applications, a series of DSCs were prepared using FTO films fabricated by varying the spraying time. Control DSCs were also prepared alongside using CFTO. Finally, the assembled DSCs were characterized and cell performances were compared to evaluate the quality of FTO films. The study mainly focused on validating our hypothesis that the transparency of the FTO substrate alone is not an executive factor when optimizing the DSC performances, and translucent FTO films with carefully controlled optical and electrical properties are more effective in optimizing the DSC efficiency. In this study, a gel polymer electrolyte that does not contain any volatile solvent was utilized in order to get higher physical and chemical stability for the cell. However, it should be noted that, despite being

stable, gel electrolytes deliver lower efficiency compared to liquid electrolytes in general. Therefore, the reported efficiencies are not intended to be comparable with that of liquid electrolyte-based cells. Nevertheless, the trend observed would help to improve efficiencies in all of the photoelectrochemical solar cells.

## EXPERIMENTAL DETAILS

**Preparation of FTO Films.** First, 9.01 g of  $\text{SnCl}_4 \cdot 5\text{H}_2\text{O}$  (Sigma-Aldrich, 99%) was added to 400  $\text{cm}^3$  of isopropanol (VWR analytical grade) and the mixture was sonicated for 15 min. The solvent isopropanol was selected based on the preliminary results. Then, 2.4 g of a saturated aqueous solution of  $\text{NH}_4\text{F}$  (Sigma-Aldrich 99%) was added to the solution mentioned above and sonicated again for 15 min. Then, a properly cleaned plain soda-lime glass substrate (1 mm  $\times$  25 mm  $\times$  25 mm) was placed on a hot plate maintained at 500  $^\circ\text{C}$ . Then, a custom-made spray gun, prepared by using two glass droppers (Figure 1a), was utilized to spray the precursor solution onto the glass substrate.

The spraying was conducted along longitudinal and lateral directions for about 10 s while maintaining a distance of 10 cm between the hot plate and the nozzle of the spray gun, such that the entire substrate is evenly covered (Figure 1b) based on previous studies.<sup>30</sup> After keeping it for  $\sim 50$  s at 500  $^\circ\text{C}$ , spraying was continued for another 10 s. This procedure was repeated until 40 mL of the precursor solution was consumed, and the sample was maintained at 500  $^\circ\text{C}$  for a further 30 min. This process, spraying 40 mL of the solution and subsequent heating to 500  $^\circ\text{C}$ , is considered a one-spray pyrolysis cycle (or one layer of the FTO film). A series of seven samples (labeled as the P-FTO series) were prepared by varying the number of FTO layers from 1 to 7 (namely, P1, P2, P3, P4, P5, P6, and P7). Three samples were prepared with each number of spray cycles (thickness) to check the reproducibility by carefully maintaining the constant spray time, sintering time, the distance between the substrate and the nozzle, the amount of precursor solution sprayed, the flow rate, and the substrate temperature. Photographs of the seven FTO samples prepared by the spray pyrolysis technique are shown in Figure 1c. The image demonstrates

the gradual drop of transparency with the increasing number of spray cycles (layers).

**Preparation of DSCs.** Then, P1, P2, P3, P4, P5, and P6 samples and a commercially available FTO substrate (CFTO) (SOLARONIX TCO10-10, thickness: 1.1 mm, sheet resistance:  $10 \Omega \square^{-1}$ , transmittance: >80% from 500 to 800 nm) of size  $1 \text{ cm} \times 2 \text{ cm}$  were used to prepare photoelectrodes for the DSC assembly. The preparation of photoelectrodes, electrolytes, counter electrodes, and DSCs was done according to an already published method.<sup>56</sup>

An FTO substrate was spin-coated with six distinct layers of  $\text{TiO}_2$  nanoparticles according to the following procedure. To produce the first layer of  $\text{TiO}_2$ , 0.5 g of  $\text{TiO}_2$  nanoparticles with an average size of 13 nm (P90 powder) was pulverized in an agate mortar with 2 mL of 0.1 M  $\text{HNO}_3$  for approximately 30 min. Half of the FTO plate was masked with scotch tape to prevent the spin coating of  $\text{TiO}_2$  on the area of FTO that will be used for electrical contacts. The resulting  $\text{TiO}_2$  slurry was then spin-coated on an FTO substrate at 2300 rpm for 2 min. After spin coating, the photoelectrode was air-dried for 5 h at ambient temperature. The sample was then placed in a furnace, the temperature of which was increased by  $50 \text{ }^\circ\text{C}$  every 10 min until it reached  $450 \text{ }^\circ\text{C}$ . The sample was then sintered for 30 min at  $450 \text{ }^\circ\text{C}$ . The preceding method was repeated for the production of the second layer of  $\text{TiO}_2$ . In order to create the third layer, a  $\text{TiO}_2$  dispersion is made by combining 0.5 g of nanoparticles with a size of 21 nm (P25 powder) and 2 mL of 0.1 M  $\text{HNO}_3$  in an agate mortar. The resulting slurry was spin-coated at 1000 rpm for 2 min and then subjected to the same air drying and sintering process as the first and second layers. Before the spin coating process for the fourth, fifth, and sixth layers, 0.1 g of poly(ethylene glycol) (PEG (MW = 4000)) and a few droplets of Triton X 100 (surfactant) were added to the  $\text{TiO}_2$  slurry and thoroughly mixed. Photoelectrodes were immersed in a 0.3 mM ethanol solution of N719 ruthenium dye [di-tetrabutylammonium cis-bis(isothiocyanato)bis(2,2'-bipyridyl-4,4'-dicarboxylate) ruthenium (II)] for approximately 24 h. Before immersion, the electrodes and the dye solution were heated to 100 and  $60 \text{ }^\circ\text{C}$ , respectively. After the electrodes were removed from the dye solution, they were carefully washed with ethanol to remove any dye molecules and particles that had become loosely attached to the FTO area, which was used for electrical contact, and the upper surface of the light irradiating area.

The electrolyte was composed of poly(ethylene oxide) (PEO), ethylene carbonate (EC), propylene carbonate (PC), 1-butyl-3-methylimidazolium iodide (BMII), propylene carbonate (PC), 1-butyl-3-methylimidazolium iodide (BMII), 4-*tert*-butylpyridine (4TBP), tetrahexylammonium iodide (Hex4NI), lithium iodide, and iodine. First, 400 mg of EC and 463.5 mg of PC were combined in a glass container with a lid. The mixture was stirred well to get a homogeneous mixture. Then, 13, 8, 18, 43, and 50 mg of 4TBP, BMII, LiI, Hex<sub>4</sub>NI, and PEO were added to the mixture, respectively, while continuing the stirring. The mixture was then heated to about  $100 \text{ }^\circ\text{C}$  under continuous stirring until it became a transparent slurry. Subsequently, 6 mg of  $\text{I}_2$  was added to the slurry under continuous stirring after the mixture was cooled down to  $\sim 40 \text{ }^\circ\text{C}$ . After that, the mixer was kept for 24 h for stabilization before using it.

A series of 6 different DSCs were assembled by sandwiching the gel polymer electrolyte between platinum (Pt) counter electrodes and dye-sensitized photoelectrodes. The cells were prepared without any electrolyte leakage or any direct contact between the Pt electrode and FTO through the electrolyte. As a reference, a DSC was prepared using the CFTO-based dye-sensitized photoelectrode. The final configuration of each DSC was [glass/FTO/ $\text{TiO}_2$ /N719 dye/gel polymer electrolyte/Pt counter electrode].

**Characterization of the FTO Series.** The sheet resistance of each sample and the commercial FTO were measured using a four-probe setup via a VK-PA-25 PV power analyzer. The measurements were taken along the two perpendicular directions parallel to the edges of the sample. The transmittance of each FTO sample was measured using a double-beam UV–visible spectrophotometer (UV-1800 series). The glass substrate was used as the reference, and the spectrum was obtained within the 300–900 nm wavelength range. For comparison, the transmittance spectra of a commercial FTO glass

(CFTO) and the soda-lime substrate glass were obtained within the same wavelength range. XRD spectra of FTO samples with layers 2, 4, and 6 and CFTO were obtained using  $\text{Cu-K}\alpha = 1.5405 \text{ \AA}$  radiation of a Rigaku Ultima IV X-ray diffractometer (KYOWAGLAS-XA) within the  $20\text{--}90^\circ$  angular range. Scanning electron microscopic (SEM) images of the surface and cross sections of the FTO samples after each spray cycle and CFTO reference were taken by using an EVO LS 15 scanning electron microscope.

**Characterization of the DSC Series.** Fabricated solar cells were irradiated with a light of  $1000 \text{ W m}^{-2}$  (AM 1.5) by a PEC-LO1 solar simulator, and the current–voltage ( $I$ – $V$ ) characteristics of the cells were obtained. The active area of a cell was  $19 \text{ mm}^2$ . Current–voltage data were measured for 3 h (at 10 min steps) under continuous irradiation. Nyquist plots of the fabricated DSCs were obtained using a Metrohm Autolab potentiostat by keeping the direct current (DC) potential set at the maximum open circuit voltage ( $V_{\text{oc}}$ ) and setting the alternative current (AC) amplitude as 0.01 V in a frequency range from 0.01 to  $10^6 \text{ Hz}$ .

## RESULTS AND DISCUSSION

**Charge Transport.** The variation of sheet resistance and conductivity of the prepared FTO films as a function of the number of spray cycles (layers) are shown in Figure 2. As expected, the sheet resistance ( $R_{\text{sh}}$ ) of the FTO films decreased gradually with the increasing number of layers (Figure 2a), as a result of the increase in the film thickness. The  $R_{\text{sh}}$  of  $13.6 \Omega$

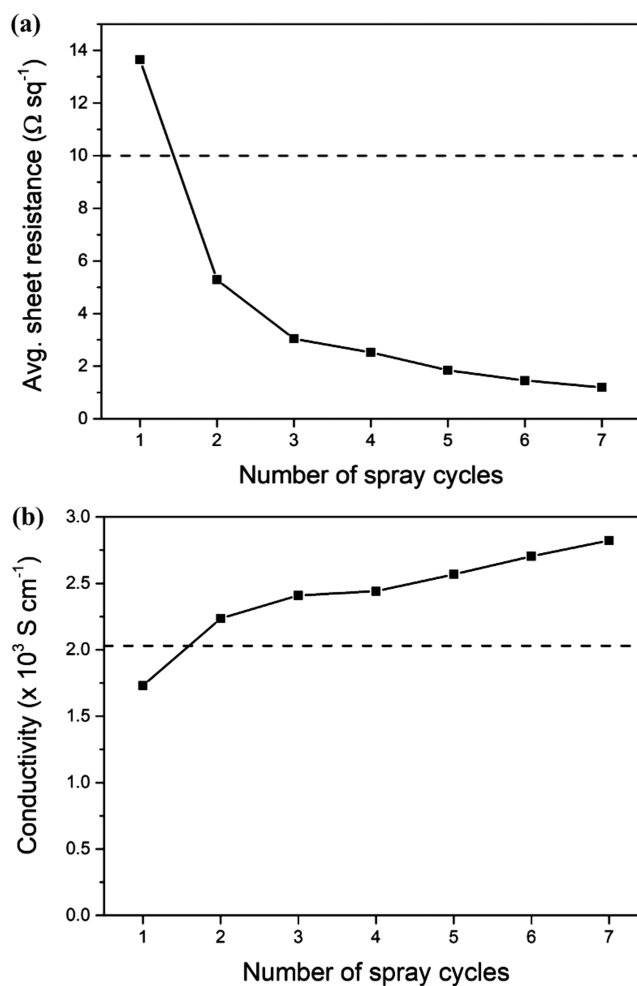


**Figure 2.** Variation of (a) sheet resistance and (b) conductivity of the prepared FTO series with the number of spray cycles (the dotted lines represent the corresponding values for the CFTO reference).

$\square^{-1}$  for the single layer (P1) was possible to be improved to  $1.20 \Omega \square^{-1}$  by increasing the number of layers up to 7 (Table 1). The observed low sheet resistance of around  $1 \Omega \square^{-1}$  is a

**Table 1. Average Values of Sheet Resistance ( $R_{sh}$ ), Conductivity ( $\sigma$ ), and Transmittance within the 380–700 nm Range ( $T_{380-700\%}$ ) of the CFTO and P-FTO Series**

photoelectrode	$R_{sh}$ of FTO ( $\Omega \square^{-1}$ )	$\sigma$ ( $\times 10^3 \text{ S cm}^{-1}$ )	$T_{380-700\%}$
CFTO	$10^a$	2.03	$82.9 \pm 0.1$
P1	$13.6 \pm 0.31$	$1.73 \pm 0.04$	$76.5 \pm 0.1$
P2	$5.28 \pm 0.12$	$2.24 \pm 0.05$	$58.2 \pm 0.3$
P3	$3.27 \pm 0.02$	$2.41 \pm 0.02$	$34.2 \pm 0.4$
P4	$2.42 \pm 0.01$	$2.44 \pm 0.01$	$7.9 \pm 0.1$
P5	$1.84 \pm 0.02$	$2.57 \pm 0.04$	$7.0 \pm 0.1$
P6	$1.46 \pm 0.02$	$2.70 \pm 0.05$	$4.5 \pm 0.1$
P7	$1.20 \pm 0.01$	$2.82 \pm 0.02$	$4.2 \pm 0.1$

<sup>a</sup>Manufacturer specifications for SOLARONIX TCO10-10.

promising value for an FTO film. This thus gives a suitable way of preparing inert electrodes with high conductivity for a variety of electrochemical device applications.<sup>57,58</sup> The sheet resistance and the conductivity of CFTO are marked in Figure 2 using dotted lines as reference values. Except for the P1, every other sample showed sheet resistance below the sheet resistance of the reference CFTO ( $10 \Omega \square^{-1}$ ). The conductivities ( $\sigma$ ) of the sample in the series, including CFTO, were calculated using the formula

$$\sigma = \frac{1}{R_{sh}t} \quad (1)$$

where  $t$  is the thickness of the FTO film, which was found from the SEM images of the film cross section.

As shown in Figure 2b, the conductivity also increased with the number of spray cycles. This may be due to the increase in crystallinity and particle size with the increasing number of layers (Tables 2 and 3). The conductivities of the prepared FTO series were above the CFTO sample except for the P1. The conductivity and sheet resistance in CFTO lie between that of the P1 and P2 samples.

**UV–Visible Absorption.** The transmittance ( $T$ ) of the FTO series (measured with reference to the blank soda-lime glass substrate) decays dramatically with the number of layers (Figure 3a). The average transmittance values of FTO samples within the 380–700 nm range ( $T_{380-700\%}$ ) were calculated using the UV–visible absorption spectra (Figure 3a), which are given in Table 1. The highest transmittance of 76% was given

**Table 3. Average Particle Size and Thickness of the FTO Samples**

sample name	avg. particle size (nm)	avg. film thickness (nm)
CFTO	$108 \pm 6$	$494 \pm 5$
P1	$179 \pm 11$	$477 \pm 8$
P2	$216 \pm 11$	$838 \pm 17$
P3	$276 \pm 14$	$1330 \pm 21$
P4	$360 \pm 30$	$1709 \pm 15$
P5	$377 \pm 29$	$2268 \pm 26$
P6	$380 \pm 30$	$2566 \pm 27$
P7	$414 \pm 25$	$2815 \pm 32$

by the sample P1. However, it is a relatively low value compared to the standard commercial sample that transmits 82% throughout the visible range (Figure 3b). Though the  $R_{sh}$  of single-layer FTO is the highest ( $13.6 \Omega \square^{-1}$ ), the highest transmittance of about 76% is exhibited by sample P1 out of fabricated samples. Conversely, the  $R_{sh}$  value of the 7-layer FTO sample is the lowest ( $1.20 \Omega \square^{-1}$ ) among observed, despite the fact that the transmittance of the sample is very low (4.2%). Therefore, about 95% of the light in the visible range is either absorbed or scattered. Further, when the number of layers is higher than 3, the transmittance is below 10%; thus—according to the standard guidelines—these FTO films are not suitable for preparing DSCs.<sup>38</sup>

The UV–visible data were used to plot the corresponding Tauc plots, utilizing the equation for direct band-gap systems

$$(\alpha h\nu)^2 = C(h\nu - E_g) \quad (2)$$

where  $\alpha$ ,  $E_g$ ,  $C$ , and  $h\nu$  are the absorption coefficient, optical band gap, an energy-independent constant, and the incident photon energy, respectively.<sup>26,59</sup> The optical band-gap value of the whole P-FTO series was around 3.75 eV ( $\sim 330$  nm), and it was a little bit lower than the band-gap value of the CFTO reference, which was found as 3.87 eV ( $\sim 320$  nm). According to the Tauc plot for P1 (Figure 3c), its optical band gap was 3.78 eV ( $\sim 328$  nm), which is higher than the energy of visible light and most of the UV light photons.

According to the calculated band gap, in principle, any absorption by the FTO film is not possible for wavelengths above 350 nm. Therefore, the drop of transmittance in the visible 350–900 nm range can mainly be attributed to the scattering effects of the FTO film. Further, the ripples visible in the 400–850 nm range for the single- and double-layer samples can be attributed to the constructive and destructive interferences due to the comparable wavelengths due to the

**Table 2. Calculated Crystallite Sizes Using the Diffraction Peaks**

crystal plane	crystallite size - $L$ (nm)			
	CFTO	P2	P4	P6
(110)	$15.51 \pm 0.24$	$10.97 \pm 0.27$	$13.97 \pm 0.15$	$17.45 \pm 0.25$
(101)	$15.04 \pm 1.22$	$10.50 \pm 0.79$	$15.49 \pm 0.30$	$15.57 \pm 0.57$
(200)	$20.23 \pm 0.12$	$25.49 \pm 0.05$	$25.87 \pm 0.08$	$25.83 \pm 0.05$
(211)	$21.11 \pm 0.76$	$15.79 \pm 1.59$	$16.29 \pm 0.43$	$18.55 \pm 0.69$
(220)	$23.52 \pm 3.34$	$7.14 \pm 2.30$	$19.17 \pm 3.18$	$19.42 \pm 3.65$
(310)	$12.02 \pm 0.56$	$9.77 \pm 0.25$	$11.96 \pm 0.58$	$15.32 \pm 1.02$
(301)	$16.23 \pm 0.59$	$11.12 \pm 1.88$	$17.46 \pm 0.84$	$17.14 \pm 0.88$
(400)	$13.60 \pm 1.97$	$18.08 \pm 0.68$	$18.59 \pm 0.88$	$18.36 \pm 0.36$
weighted average of $L$ (nm)	18.53	23.55	22.01	24.32
crystallinity ( $X_c$ )%	69.42	74.10	77.22	83.17

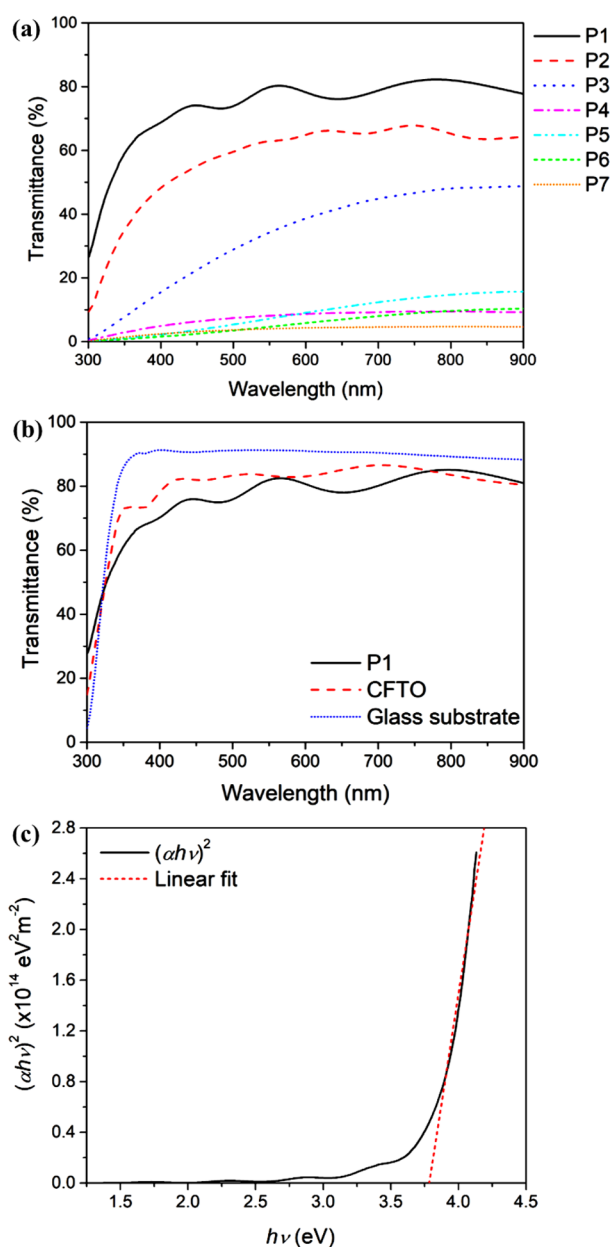


**Figure 3.** (a) Transmittance spectra for the P-FTO series. (b) Comparison between transmittance spectra for the P1 sample, the blank soda-lime glass substrate, and the CFTO reference. (c) Tauc plot for the P1 sample.

differences in film thickness and refractive index between the FTO layers and the glass substrate. The ripples red-shifted when increasing layer thickness and vanished for the thicker samples.

**Structural Properties.** The XRD spectra and identified crystallographic planes are given in Figure 4. As expected, the intensity of the peaks has increased with the increasing number of spray cycles. In addition, the XRD spectra suggest no significant differences between the structure of FTO between the P-FTO series and the commercial FTO reference. The crystallite size ( $L$ ) related to each peak was calculated by fitting to Scherrer's equation

$$L = \frac{K\lambda}{W \cos(\theta)} \quad (3)$$

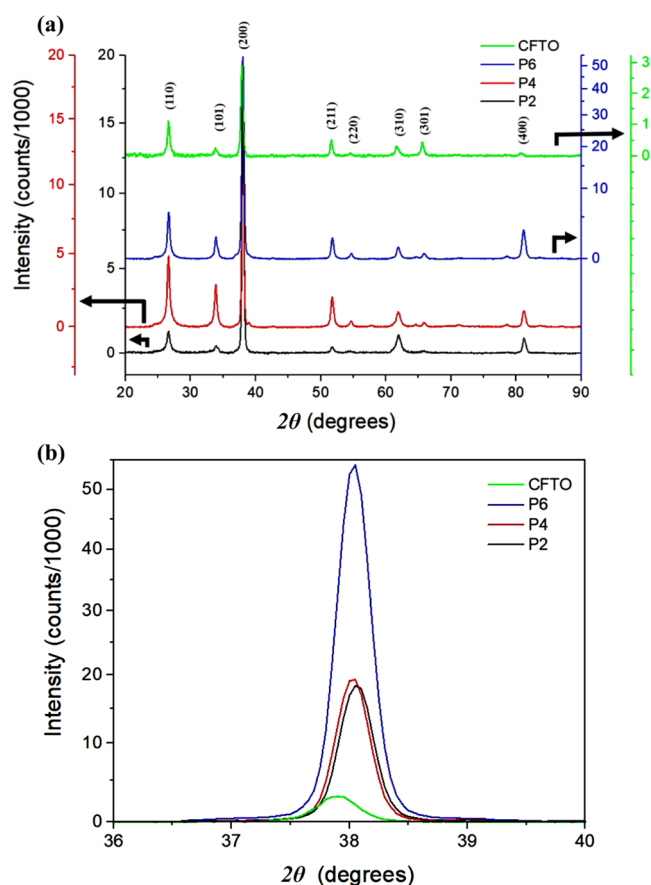


**Figure 4.** (a) Comparison of XRD patterns of P2, P4, P6, and CFTO [vertical axis color-coded]. (b) Enlarged view of (200) peaks.

where  $\lambda$  is the X-ray wavelength,  $\theta$  is Bragg's angle,  $K$  is a dimensionless constant from the assumptions made in theory (taken as 0.9 in this study),<sup>60,61</sup> and  $W$  is the full width at half-maximum of the peak. Calculated crystallite sizes using the diffraction peaks related to eight crystal planes are given in Table 2. The crystallite size related to almost all of the crystal planes of the fabricated P-FTO series gradually increased with the layer count. When the peaks were scrutinized, peak narrowing was observed due to the formation of larger crystallites with the increase in the number of spray cycles. The crystallinity percentage ( $X_c$ ) of each sample was calculated using the equation

$$X_c = \frac{A_c}{A} \times 100\% \quad (4)$$

where  $A_c$  is the summation of the area under the curve of each crystalline peak and  $A$  is the total area under the curve of the XRD spectrum.<sup>62,63</sup>

The increase of crystallinity with the number of layers (Table 2) can be a reason for the observed increase in conductivity with the increasing number of spray cycles. The weighted averaged crystallite sizes and crystallinity percentage of the P-FTO samples are considerably higher than that of CFTO, which may be the reason for the higher conductivity of the P-FTO series.

**Surface Morphology and the Thickness.** SEM images of the surfaces and cross sections of the FTO samples with spray cycles 2, 4, and 6, along with the CFTO reference, are shown in Figure 5. According to the scanning electron

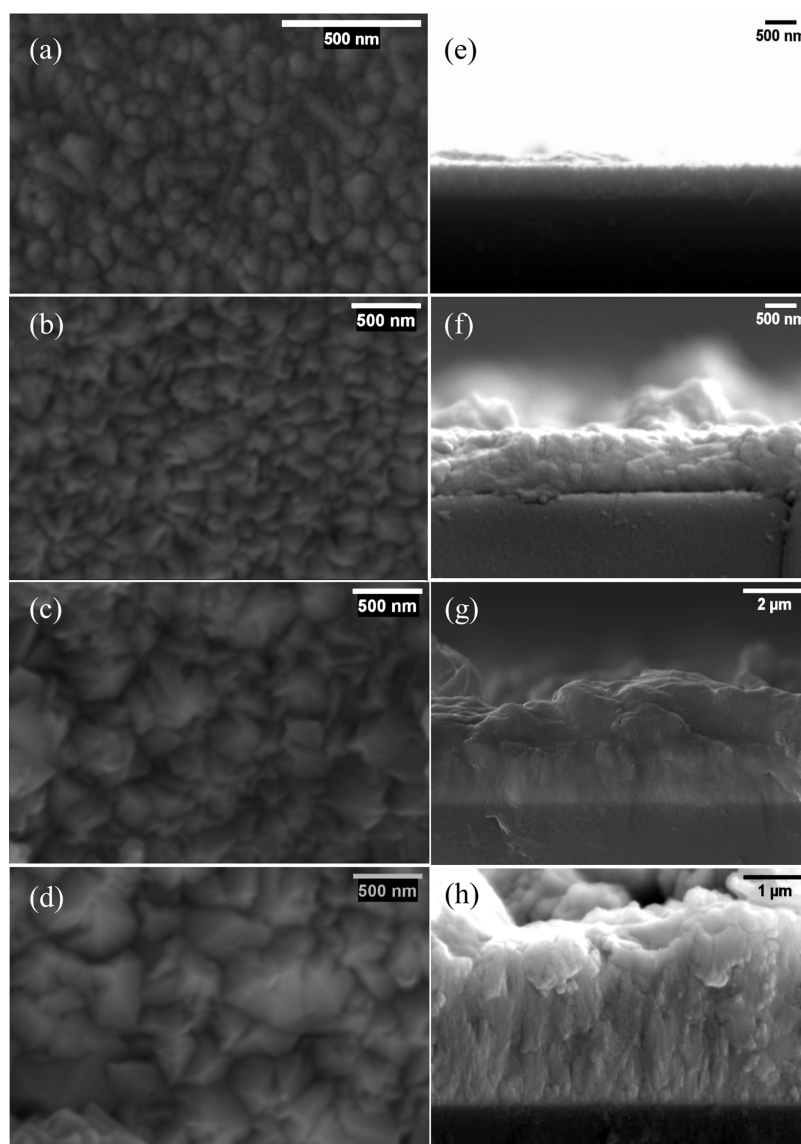


**Figure 5.** SEM images of surface morphology of (a) CFTO, (b) P2, (c) P4, and (d) P6 samples. Panels (e), (f), (g), (h) represent their cross sections.

micrographs, the particle size of FTO samples prepared in this work increases with the increasing number of spray cycles (Figure 5). As a result of that, the apparent roughness of the surface has increased. Further, this fact is also corroborated by the disappearance of ripples with the increase in the number of spray cycles in the UV–visible transmittance spectra shown in Figure 3a, where ripples are an indication of the smoothness of the thin film.<sup>64</sup> The ripples in the 400–850 nm range correspond to the constructive and destructive interferences related to the film thickness and the contrast of the refractive index between the SnO<sub>2</sub> film and the substrate. The improved roughness gives an added advantage in increasing the contact area with TiO<sub>2</sub> semiconductor nanoparticles when these FTO films are used in DSCs, leading to improved interfacial charge transfer and enhanced shear strength between FTO and TiO<sub>2</sub> films. The estimated average particle size and the FTO film thickness are given in Table 3. In addition, in order to check the reproducibility of layer thickness, the average layer thickness deposited by a spray cycle is estimated. It was observed that the average thickness of the FTO layer deposited

per cycle is 435 nm with a standard deviation of 25 nm, indicating the high reproducibility of the thickness. However, in order to get highly reproducible sheet resistance and morphology, maintaining the constant spray time, the sintering time, the distance between the substrate and nozzle, the amount of precursor solution, the flow rate, and the substrate temperature is highly important.

**Dye-Sensitized Solar Cells.** DSCs were fabricated using the P-FTO series and CFTO reference by incorporating them into the photoelectrodes in order to probe photovoltaic conversion parameters. The photocurrent density against cell potential ( $J-V$ ) and power density against cell potential ( $P_d-V$ ) with irradiation time are presented in Figures 6 and 7, respectively. As evident from the  $J-V$  curves, there is a gradual increase in the current density with irradiation time. A similar trend has been observed across the whole DSC series. This trend can be a result of the increase in temperature due to heating effects imposed by prolonged irradiation. Before taking the  $J-V$  measurements, the temperature of the cells was 31 °C and, after the continuous irradiation for 3 h, the cell

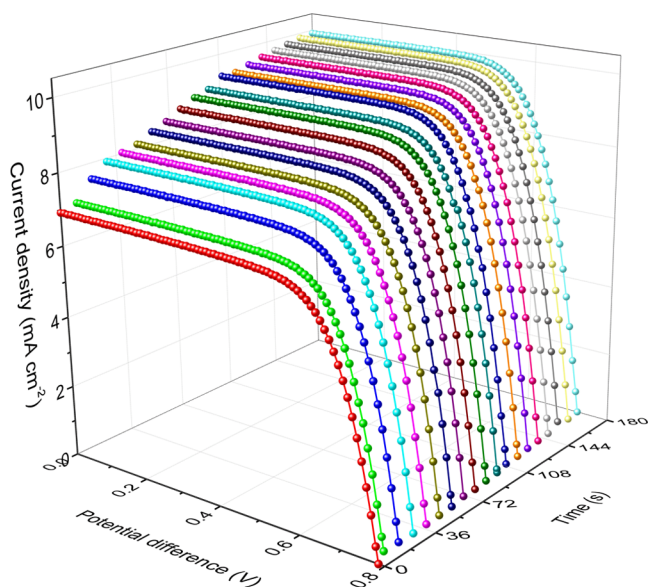


**Figure 6.** Photocurrent density vs. cell potential ( $J-V$ ) as a function of time for the P3-based DSC.

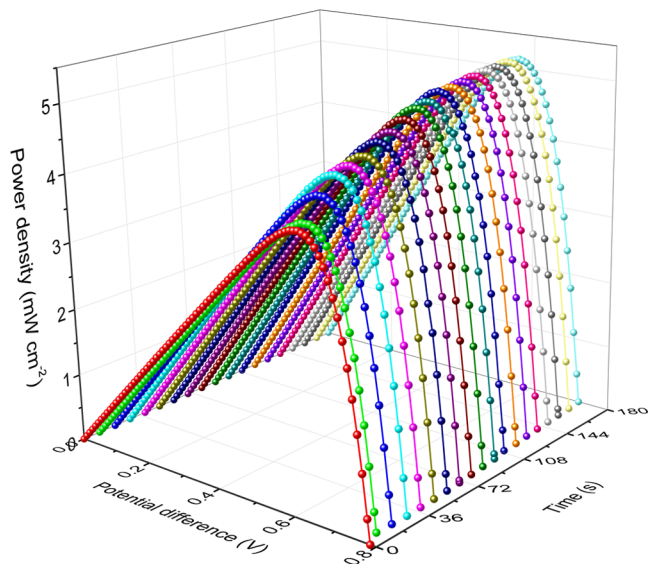


**Figure 7.** Power density vs cell potential ( $P_d-V$ ) as a function of time for the P3-based DSC.

temperature was found to be increased to about 40 °C. A slight temperature increase can cause significant conductivity enhancement in gel polymer electrolytes, resulting in cell performance enhancement.<sup>65,66</sup> Further, along with the

increase in the photocurrent, there is a slight decline in  $V_{oc}$ , which can be a result of the increased charge recombination caused by increased charge-transfer dynamics due to the increase in temperature.

One of the important observations made in this study is that all of the cells exhibited excellent stability within the investigated 3 h irradiation period. These cells are unsealed cells, and, in the present study, gel polymer electrolytes free of volatile solvent were used, expecting higher stability.<sup>41,67</sup> The merit of selecting the appropriate electrolyte and electrode is reflected by the excellent short-term stability exhibited by the cells. However, since the main focus of this study is the development of FTOs suitable for DSCs, the long-term stability of these DSCs was not investigated.

The DSC performance parameters of the cells prepared using the series of FTOs are given in Table 4. The DSC fabricated with the FTO prepared using three spray cycles (sample P3), which showed an  $R_{sh}$  of  $3.27 \Omega \square^{-1}$  and an average transmittance of 34.2%, exhibited the highest cell efficiency of 5.14% with excellent stability. Though the transmittance (34.2%) is low, this cell exhibited significantly higher stability and efficiency than CFTO-based DSC, which has a higher transmittance (83%) in the visible range. These results indicate that DSCs can still be fabricated using FTO films with low transmittance and higher conductance (low  $R_{sh}$ ). In addition, all of the cells exhibited excellent fill factor (higher than 70%), which can be attributed to the lower series resistance of the cell.

Moreover, the cells prepared using the P-FTO samples showed a relatively higher efficiency despite having a transmittance of less than 10%. For example, DSCs prepared using the FTOs having very low 7.87, 6.95, and 4.48% transmittances showed 4.66, 4.35, and 3.17% energy conversion efficiencies, respectively. The relatively high efficiencies given by low transmittance FTO-based cells clearly indicate that the light scattered from the FTO has also been absorbed by the dye molecules. The suggested possible mechanism is illustrated in Figure 8. Further, from the effective scattering, the masking (shadowing) of dye molecules can be minimized; thus, more sensitizer molecules in the photoelectrode can be excited in the light-harvesting process. In addition to the improvements due to light scattering and increased dye excitation, the decreased sheet resistance would also have contributed to relatively high efficiencies for the cells prepared using low transmittance FTOs.

After showing maximum efficiency for the 3-layered FTO-based DSC, there is a decreasing trend of efficiency with the increasing number of layers. However, this drop in efficiency is smaller compared to the dramatic drop in transmittance observed with the increasing number of layers. Therefore,

**Table 4.** Short Circuit Current Density ( $J_{sc}$ ), Open Circuit Voltage ( $V_{oc}$ ), Fill Factor (FF), Average Cell Efficiency ( $\eta$  %), and Maximum Cell Efficiency ( $\eta_{max}$  %) of the Corresponding DSC Series

photoelectrode	$J_{sc}$ (mA cm <sup>-2</sup> )	$V_{oc}$ (mV)	FF%	avg. $\eta$ %	$\eta_{max}$ %
CFTO	$7.78 \pm 0.27$	$744 \pm 3$	$72.4 \pm 0.2$	$4.17 \pm 0.11$	4.74
P1	$7.95 \pm 0.15$	$702 \pm 3$	$70.6 \pm 0.1$	$3.93 \pm 0.05$	4.14
P2	$7.22 \pm 0.30$	$768 \pm 5$	$75.1 \pm 0.3$	$4.14 \pm 0.12$	4.65
P3	$8.75 \pm 0.22$	$752 \pm 4$	$72.7 \pm 0.2$	$4.77 \pm 0.09$	5.14
P4	$8.76 \pm 0.18$	$696 \pm 2$	$71.8 \pm 0.2$	$4.36 \pm 0.07$	4.66
P5	$7.87 \pm 0.20$	$708 \pm 5$	$71.9 \pm 0.1$	$3.99 \pm 0.07$	4.35
P6	$5.55 \pm 0.09$	$759 \pm 4$	$72.3 \pm 0.1$	$3.04 \pm 0.03$	3.17

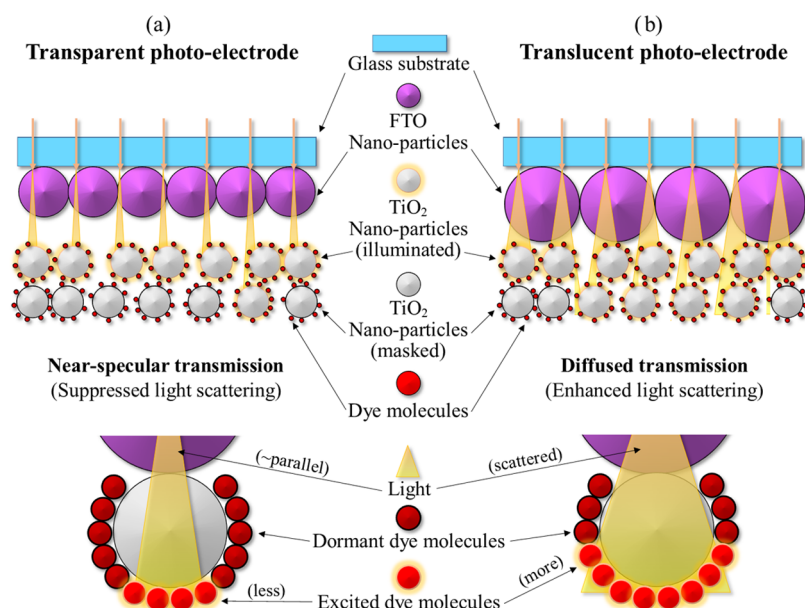


**Figure 8.** Schematic illustration of the (b) reduced multilayer light masking and enhanced light scattering effects due to a translucent photoelectrode compared with (a) a standard transparent photoelectrode.

these small efficiency drops shown with the increase in layer thickness can be attributed to the increase in light attenuation. It seems that up to 3 layers, the positive contribution from the improved conductance (reduced sheet resistance) and the scattering effects is more significant toward the efficiency than the competing negative contribution due to the attenuation effects of light.

Haacke's figure of merit ( $\Phi$ ) for the photovoltaic application of transparent conducting films is defined as

$$\Phi = \frac{T^{10}}{R_{sh}} \quad (5)$$

where  $T$  and  $R_{sh}$  are the transmittance and the sheet resistance, respectively.<sup>68,69</sup> High  $\Phi$  values are preferred for photovoltaic applications. However, this figure-of-merit value for CFTO was about  $1.30 \times 10^{-2} \Omega^{-1}$ , while for the sample P3 it was about  $7.19 \times 10^{-6} \Omega^{-1}$ , which is  $\sim 10^4$  times smaller. This indicates that, when it comes to dye-sensitized solar cell applications, Haacke's figure-of-merit value of the FTO substrate is not a crucial parameter.

Nyquist's plot of the prepared DSC series is shown in Figure 9a. Generally, three semicircles can be observed in the impedance spectroscopy data obtained for DSCs under standard biasing conditions.<sup>70</sup> Nyquist's plots show traces of overlapping among 2 or 3 semicircles.

The small semicircle of Nyquist's plot on the left side (high-frequency region) is approximately identical for the whole DSC series, representing the resistance for the charge transfer between the platinum counter electrode and the gel polymer electrolyte.<sup>71</sup> This behavior is expected since the electrolytes and counter electrodes were invariant in this study. On Nyquist plots, the diameter of the large semicircle in the low-frequency region (right side) is related to the charge-transfer resistance  $R_{ct}$  at the photoelectrode/electrolyte interface and ion transport in the bulk of the electrolyte. Further, the variation in the size of the large semicircle can result from the variation of the applied potential difference, which is similar to the cell potential in this case.<sup>72</sup> For example, Figure 9c shows

the variation of Nyquist plots of P2-FTO-based DSC under different applied potentials. According to that, the diameters of the second semicircle of Nyquist's plots have been decreased with the increase in the applied potential difference across the cell.

The first intercept of the curve with the real axis is related to the resistance ( $R_s$ ) of the current collectors and the leads. As shown in Figure 9a, this intersecting point shifts to the left side with the reduction of the sheet resistance of the FTO substrate. This indicates the decrease in resistance with the increase in the thickness of the FTO film. The CFTO-based DSC also follows this pattern while having a sheet resistance value between P1 and P2. Notably, the sheet resistance of the FTO film and the corresponding  $R_s$  values show a linear relationship, as in Figure 9b. A similar relationship has been reported by Han et al. as well.<sup>72</sup>

In the commercialization of solar cells, one of the key challenges is the "module resistance", which includes the resistance of the transparent conducting oxide substrate. In particular, the higher the substrate resistance, the lower the fill factor is. Therefore, in practical solar panels, charge collector grids are used in order to minimize the internal module series resistance and maintain the fill factor. However, by using high-conducting FTOs as current collectors (substrate), the necessity of an additional metal grid can be entirely eliminated or larger grids can be used.

In order to get a clear comparison, the transmittance, sheet resistance of FTO, and the efficiencies of DSCs are plotted in Figure 10.

## CONCLUSIONS

We have shown that it is possible to reduce the sheet resistance of FTO films up to  $\sim 1 \Omega \square^{-1}$  while keeping the resistivity around  $3.54 \times 10^{-4} \Omega \text{ cm}$ , using a facile spray pyrolysis technique. As evident by the performance of the DSCs prepared using fabricated FTO films with the said method, better energy conversion efficiencies can be obtained with low-transparency FTO films having low sheet resistance compared

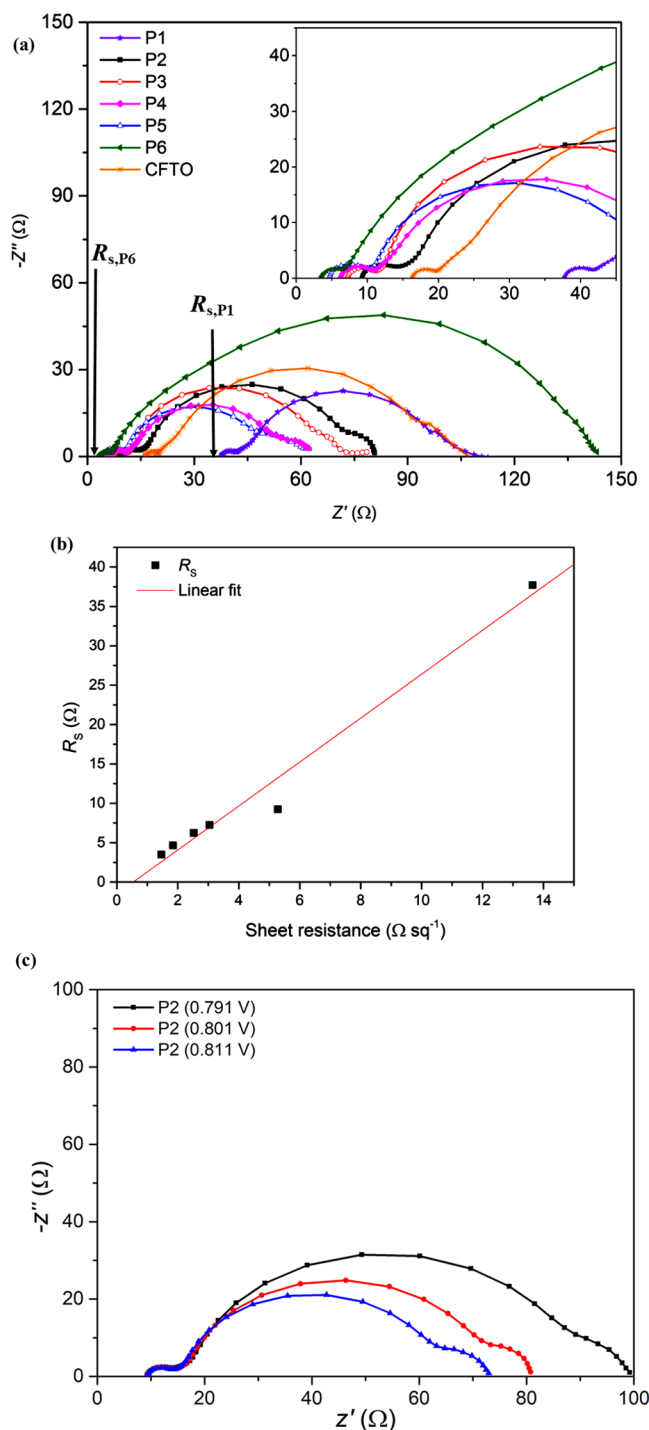


**Figure 9.** (a) Comparison of Nyquist's plots of prepared DSC series. Inset: zoomed region of the same Nyquist's plot ( $Z'$ : the real part of the impedance,  $Z''$ : the imaginary part of the impedance). (b) Graph of  $R_s$  vs sheet resistance values for the P-FTO series. (c) Comparison of Nyquist's plots of P2-FTO-based DSC under different applied potentials.

to conventional, highly transparent films. For example, DSCs prepared using the FTO substrates having very low 7.9, 7.0, and 4.5% transmittances have shown 4.66, 4.35, and 3.17% energy conversion efficiencies, respectively. The highest recorded energy conversion efficiency of 5.14% was obtained for the FTO film with a 34.2% transmittance and a  $3.27 \Omega \square^{-1}$  sheet resistance, and it was considerably higher than that of

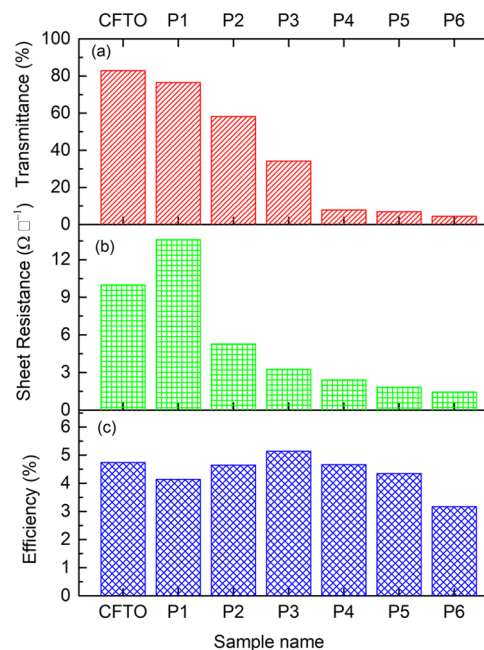


**Figure 10.** Comparison of (a) transmittance, (b) sheet resistance, and (c) solar cell efficiency for commercial (CFTO) and fabricated (P-FTO) samples.

standard commercial FTO films (4.74%) with an  $\sim 83\%$  transmittance and a  $10 \Omega \square^{-1}$  sheet resistance. The results indicate that the optical transparency of FTO is not a dominant factor, and translucent FTO films with carefully engineered light scattering properties can be used in fabricating dye solar cells with superior efficiency. In addition, the stability with respect to the irradiation time and fill factor is much better for such films compared to the standard commercial FTO substrates with high transparency and average sheet resistance.

## AUTHOR INFORMATION

### Corresponding Author

Thennakoon Mudiyansele Wijendra Jayalath

Bandara – Department of Physics and Postgraduate Institute of Science, Faculty of Science, University of Peradeniya, Peradeniya 20400, Sri Lanka; [orcid.org/0000-0003-1659-3042](https://orcid.org/0000-0003-1659-3042); Email: [wijendra@sci.pdn.ac.lk](mailto:wijendra@sci.pdn.ac.lk)

### Authors

Roshan Sudarshana Rathnayaka Kananke Udubokke

Rathnayakage – Department of Physics and Postgraduate Institute of Science, Faculty of Science, University of Peradeniya, Peradeniya 20400, Sri Lanka; [orcid.org/0000-0001-6486-2871](https://orcid.org/0000-0001-6486-2871)

Kapila Wijayarathne – Department of Physics and Postgraduate Institute of Science, Faculty of Science, University of Peradeniya, Peradeniya 20400, Sri Lanka

Gamaralalage Rajanya Asoka Kumara – National Institute of Fundamental Studies, Kandy 20000, Sri Lanka; [orcid.org/0000-0001-9804-2652](https://orcid.org/0000-0001-9804-2652)

Landewatte Ajith de Silva – Department of Physics, University of West Georgia, Carrollton 30118 Georgia, United States; [orcid.org/0000-0003-1990-5654](https://orcid.org/0000-0003-1990-5654)

Kirithi Tennakone – National Institute of Fundamental Studies, Kandy 20000, Sri Lanka; Department of Physics,

Georgia State University, 30302 Atlanta, Georgia, United States

Complete contact information is available at:  
<https://pubs.acs.org/10.1021/acsaem.3c00058>

## Notes

The authors declare no competing financial interest.

## ACKNOWLEDGMENTS

The authors gratefully acknowledge the funding received from the Postgraduate Institute of Science (PGIS) research grant (No. PGIS/2020/05) and the University of Peradeniya research grant (No. URG/2023/34/S). The assistance provided by Mr. A.M.M.C. Abeysinghe at the Workshop of the Faculty of Science managed by the Department of Physics, University of Peradeniya, Sri Lanka, is recognized.

## REFERENCES

- (1) Ho, I. H.; Chang, C.-W.; Chen, Y.-L.; Chang, W.-Y.; Kuo, T.-J.; Lu, Y.-J.; Gwo, S.; Ahn, H. Ultrathin TiN Epitaxial Films as Transparent Conductive Electrodes. *ACS Appl. Mater. Interfaces* **2022**, *14*, 16839–16845.
- (2) Kim, J.; Kendall, O.; Ren, J.; Billy, J. M.; McConville, C. F.; van Embden, J.; Gaspera, E. D. Highly Conductive and Visibly Transparent P-Type CuCrO<sub>2</sub> Films by Ultrasonic Spray Pyrolysis. *ACS Appl. Mater. Interfaces* **2022**, *14*, 11768–11778.
- (3) Ellmer, K.; Klein, A.; Rech, B. *Transparent Conductive Zinc Oxide Basics and Applications in Thin Film Solar Cells*; Springer: Verlag Berlin Heidelberg, 2008.
- (4) Young, N. D.; Bunn, R. M.; Wilks, R. W.; McCulloch, D. J.; Deane, S. C.; Edwards, M. J.; Harkin, G.; Pearson, A. D. Thin Film Transistor Diode Addressed AMLCDs on Polymer Substrates. *J. Soc. Inf. Disp.* **1997**, *5*, 275–281.
- (5) Kim, K.; Park, N.; Kim, T.; Cho, K. S.; Lee, J.; et al. Indium Tin Oxide Thin Films Grown on Polyethersulphone (PES) Substrates by Pulsed-Laser Deposition for Use in Organic Light-Emitting Diodes. *ETRI J.* **2005**, *27*, 405–410.
- (6) Presley, R. E.; Munsee, C. L.; Park, C.; Hong, D.; Wager, J. F.; Keszler, D. A. Tin Oxide Transparent Thin-Film Transistors. *J. Phys. D: Appl. Phys.* **2004**, *37*, 2810–2813.
- (7) Betz, U.; Kharrazi Olsson, M.; Marthy, J.; Escolá, M. F.; Atamny, F. Thin Films Engineering of Indium Tin Oxide: Large Area Flat Panel Displays Application. *Surf. Coat. Technol.* **2006**, *200*, 5751–5759.
- (8) Minami, T. Transparent Conducting Oxide Semiconductors for Transparent Electrodes. *Semicond. Sci. Technol.* **2005**, *20*, S35.
- (9) Madelung, O. *Semiconductors: Data Hand Book*, 3rd ed.; Springer-Verlag: Berlin Heidelberg, New York, 2004.
- (10) Batzill, M.; Diebold, U. The Surface and Materials Science of Tin Oxide. *Prog. Surf. Sci.* **2005**, *79*, 47–154.
- (11) Bansal, S.; Pandya, D. K.; Kashyap, S. C. Charge Transport Mechanism in High Conductivity Undoped Tin Oxide Thin Films Deposited by Reactive Sputtering. *Thin Solid Films* **2012**, *524*, 30–34.
- (12) Huh, M. S.; Yang, B. S.; Lee, J.; Heo, J.; Han, S. J.; Yoon, K.; Yang, S. H.; Hwang, C. S.; Kim, H. J. Improved Electrical Properties of Tin-Oxide Films by Using Ultralow-Pressure Sputtering Process. *Thin Solid Films* **2009**, *518*, 1170–1173.
- (13) Brousseau, J. L.; Bourque, H.; Tessier, A.; Leblanc, R. M. Electrical Properties and Topography of SnO<sub>2</sub> Thin Films Prepared by Reactive Sputtering. *Appl. Surf. Sci.* **1997**, *108*, 351–358.
- (14) Dominguez, J. E.; Fu, L.; Pan, X. Q. Effect of Crystal Defects on the Electrical Properties in Epitaxial Tin Dioxide Thin Films. *Appl. Phys. Lett.* **2002**, *81*, 5168–5170.
- (15) Thangaraju, B. Structural and Electrical Studies on Highly Conducting Spray Deposited Fluorine and Antimony Doped SnO<sub>2</sub> Thin Films from SnCl<sub>2</sub> Precursor. *Thin Solid Films* **2002**, *402*, 71–78.
- (16) Agashe, C.; Major, S. S. The Effect of F, Cl and Br Doping on the Growth and Structural Properties of Sprayed SnO<sub>2</sub> Films. *J. Phys. D: Appl. Phys.* **1996**, *29*, 2988–2991.
- (17) Sarker, S.; Seo, H. W.; Jin, Y. K.; Aziz, M. A.; Kim, D. M. Transparent Conducting Oxides and Their Performance as Substrates for Counter Electrodes of Dye-Sensitized Solar Cells. *Mater. Sci. Semicond. Process.* **2019**, *93*, 28–35.
- (18) Martínez, A. I.; Huerta, L.; O-Rueda De León, J. M.; Acosta, D.; Malik, O.; Aguilar, M. Physicochemical Characteristics of Fluorine Doped Tin Oxide Films. *J. Phys. D: Appl. Phys.* **2006**, *39*, S091–S096.
- (19) Rakhshani, A. E.; Makhdisi, Y.; Ramazaniyan, H. A. Electronic and Optical Properties of Fluorine-Doped Tin Oxide Films. *J. Appl. Phys.* **1998**, *83*, 1049–1057.
- (20) Shewale, P. S.; Patil, S. I.; Uplane, M. D. Preparation of Fluorine-Doped Tin Oxide Films at Low Substrate Temperature by an Advanced Spray Pyrolysis Technique, and Their Characterization. *Semicond. Sci. Technol.* **2010**, *25*, No. 115008.
- (21) Rey, G.; Ternon, C.; Modreanu, M.; Mescot, X.; Consonni, V.; Bellet, D. Electron Scattering Mechanisms in Fluorine-Doped SnO<sub>2</sub> Thin Films. *J. Appl. Phys.* **2013**, *114*, No. 183713.
- (22) Aouaj, M. A.; Diaz, R.; Belayachi, A.; Rueda, F.; Abd-Lefdil, M. Comparative Study of ITO and FTO Thin Films Grown by Spray Pyrolysis. *Mater. Res. Bull.* **2009**, *44*, 1458–1461.
- (23) Kim, H.; Auyeung, R. C. Y.; Piqué, A. Transparent Conducting F-Doped SnO<sub>2</sub> Thin Films Grown by Pulsed Laser Deposition. *Thin Solid Films* **2008**, *516*, S052–S056.
- (24) Noor, N.; Parkin, I. P. Enhanced Transparent-Conducting Fluorine-Doped Tin Oxide Films Formed by Aerosol-Assisted Chemical Vapour Deposition. *J. Mater. Chem. C* **2013**, *1*, 984–996.
- (25) Morán-Pedroso, M.; Gago, R.; Julin, J.; Salas-Colera, E.; Jimenez, I.; De Andrés, A.; Prieto, C. Correlated Effects of Fluorine and Hydrogen in Fluorinated Tin Oxide (FTO) Transparent Electrodes Deposited by Sputtering at Room Temperature. *Appl. Surf. Sci.* **2021**, *537*, No. 147906.
- (26) Banyamin, Z. Y.; Kelly, P. J.; West, G.; Boardman, J. Electrical and Optical Properties of Fluorine Doped Tin Oxide Thin Films Prepared by Magnetron Sputtering. *Coatings* **2014**, *4*, 732–746.
- (27) Moholkar, A. V.; Pawar, S. M.; Rajpure, K. Y.; Bhosale, C. H. Effect of Concentration of SnCl<sub>4</sub> on Sprayed Fluorine Doped Tin Oxide Thin Films. *J. Alloys Compd.* **2008**, *455*, 440–446.
- (28) Moholkar, A. V.; Pawar, S. M.; Rajpure, K. Y.; Bhosale, C. H.; Kim, J. H. Effect of Fluorine Doping on Highly Transparent Conductive Spray Deposited Nanocrystalline Tin Oxide Thin Films. *Appl. Surf. Sci.* **2009**, *255*, 9358–9364.
- (29) Elangovan, E.; Ramamurthi, K. Studies on Micro-Structural and Electrical Properties of Spray-Deposited Fluorine-Doped Tin Oxide Thin Films from Low-Cost Precursor. *Thin Solid Films* **2005**, *476*, 231–236.
- (30) Bandara, T. M. W. J.; Aththanayake, A. A. A. P.; Kumara, G. R. A.; Samarasekera, P.; DeSilva, L. A.; Tennakone, K. Transparent and Conductive F-Doped SnO<sub>2</sub> Nanostructured Thin Films by Sequential Nebulizer Spray Pyrolysis. *MRS Adv.* **2021**, *6*, 417–421.
- (31) Benhaoua, B.; Abbas, S.; Rahal, A.; Benhaoua, A.; Aida, M. S. Effect of Film Thickness on the Structural, Optical and Electrical Properties of SnO<sub>2</sub>: F Thin Films Prepared by Spray Ultrasonic for Solar Cells Applications. *Superlattices Microstruct.* **2015**, *83*, 78–88.
- (32) Kumara, G. R. A.; Ranasinghe, C. S. K.; Jayaweera, E. N.; Bandara, H. M. N.; Okuya, M.; Rajapakse, R. M. G. Preparation of Fluoride-Doped Tin Oxide Films on Soda-Lime Glass Substrates by Atomized Spray Pyrolysis Technique and Their Subsequent Use in Dye-Sensitized Solar Cells. *J. Phys. Chem. C* **2014**, *118*, 16479–16485.
- (33) Lin, C. C.; Chiang, M. C.; Chen, Y. W. Temperature Dependence of Fluorine-Doped Tin Oxide Films Produced by Ultrasonic Spray Pyrolysis. *Thin Solid Films* **2009**, *518*, 1241–1244.
- (34) Zhao, Q.; Wu, S.; Miao, D. Effect of Substrate Temperature on the Haze and Properties of SnO<sub>2</sub>: F Thin Film Coated on Glass (FTO) by Spray Pyrolysis Process. *Adv. Mater. Res.* **2011**, *151*, 1043–1048.

- (35) Kim, K.; Nam, S. K.; Moon, J. H. Dual-Band Luminescent Solar Converter-Coupled Dye-Sensitized Solar Cells for High-Performance Semitransparent Photovoltaic Device. *ACS Appl. Energy Mater.* **2020**, *3*, 5277–5284.
- (36) Pirrone, N.; Bella, F.; Hernández, S. Solar H<sub>2</sub> Production Systems: Current Status and Prospective Applications. *Green Chem.* **2022**, *24*, 5379–5402.
- (37) Herrando, M.; Pantaleo, A. M.; Wang, K.; Markides, C. N. Solar Combined Cooling, Heating and Power Systems Based on Hybrid PVT, PV or Solar-Thermal Collectors for Building Applications. *Renewable Energy* **2019**, *143*, 637–647.
- (38) Zhang, S. Study of Fluorine-Doped Tin Oxide (FTO) Thin Films for Photovoltaics Applications 2018 <https://www.theses.fr/2017GREAI021%0Ahttps://tel.archives-ouvertes.fr/tel-01689976/document>.
- (39) Peter, I. J.; Vijaya, S.; Anandan, S.; Karazhanov, S.; Nithiananthi, P. MWCNT Aided Cobalt Antimony Sulfide Electrocatalyst for Dye-Sensitized Solar Cells and Supercapacitors: Designing Integrated Photo-Powered Energy System. *J. Electrochem. Soc.* **2022**, *169*, No. 056518.
- (40) Lavagna, L.; Syrokostas, G.; Francia, C.; Bodoardo, S.; Bella, F.; Fagioliari, L.; Amici, J.; Leftheriotis, G. Platinum-Free Photoelectrochromic Devices Working with Copper-Based Electrolytes for Ultrastable Smart Windows. *J. Mater. Chem. A* **2021**, *9*, 19687–19691.
- (41) Nishshanke, G. B. M. M. M.; Arof, A. K.; Bandara, T. M. W. J. Review on Mixed Cation Effect in Gel Polymer Electrolytes for Quasi Solid-State Dye-Sensitized Solar Cells. *Ionics* **2020**, *26*, 3685–3704.
- (42) Alnoman, R. B.; Nabil, E.; Parveen, S.; Hagar, M.; Zakaria, M. UV-Selective Organic Absorbers for the Cosensitization of Greenhouse-Integrated Dye-Sensitized Solar Cells: Synthesis and Computational Study. *RSC Adv.* **2022**, *12*, 11420–11435.
- (43) Han, S. H.; Lee, S.; Shin, H.; Jung, H. S. A Quasi-Inverse Opal Layer Based on Highly Crystalline TiO<sub>2</sub> Nanoparticles: A New Light-Scattering Layer in Dye-Sensitized Solar Cells. *Adv. Energy Mater.* **2011**, *1*, 546–550.
- (44) Bonomo, M.; Zarate, A. Y. S.; Fagioliari, L.; Damin, A.; Galliano, S.; Gerbaldi, C.; Bella, F.; Barolo, C. Unreported Resistance in Charge Transport Limits the Photoconversion Efficiency of Aqueous Dye-Sensitized Solar Cells: An Electrochemical Impedance Spectroscopy Study. *Mater. Today Sustainability* **2023**, *21*, No. 100271.
- (45) Sasidharan, S.; Pradhan, S. C.; Jagadeesh, A.; Nair, B. N.; Mohamed, A. A. P.; Narayanan, N. U.; Soman, S.; Hareesh, U. N. S. Bifacial Dye-Sensitized Solar Cells with Enhanced Light Scattering and Improved Power Conversion Efficiency under Full Sun and Indoor Light Conditions. *ACS Appl. Energy Mater.* **2020**, *3*, 12584–12595.
- (46) Bandara, T. M. W. J.; Hansadi, J. M. C.; Bella, F. A Review of Textile Dye-sensitized Solar Cells for Wearable Electronics. *Ionics* **2022**, *28*, 2563–2583.
- (47) Wang, Y.; Yang, Z.; Huang, Y.; Yan, Y.; Hou, J.; Li, Z.; Cao, G. Hierarchical ZnO Microspheres Embedded in TiO<sub>2</sub> Photoanode for Enhanced CdS/CdSe Sensitized Solar Cells. *ACS Appl. Energy Mater.* **2019**, *2*, 1259–1265.
- (48) Ambapuram, M.; Ramireddy, R.; Maddala, G.; Godugunuru, S.; Yerva, P. V. S.; Mitty, R. Effective Upconverter and Light Scattering Dual Function LiYF<sub>4</sub>:Er<sup>3+</sup>/Yb<sup>3+</sup>-Assisted Photoelectrode for High Performance Cosensitized Dye Sensitized Solar Cells. *ACS Appl. Electron. Mater.* **2020**, *2*, 962–970.
- (49) Saikia, B. K.; Benoy, S. M.; Bora, M.; Tamuly, J.; Pandey, M.; Bhattacharya, D. A Brief Review on Supercapacitor Energy Storage Devices and Utilization of Natural Carbon Resources as Their Electrode Materials. *Fuel* **2020**, *282*, No. 118796.
- (50) González, A.; Goikolea, E.; Barrena, J. A.; Mysyk, R. Review on Supercapacitors: Technologies and Materials. *Renewable Sustainable Energy Rev.* **2016**, *58*, 1189–1206.
- (51) Poonam; Sharma, K.; Arora, A.; Tripathi, S. K. Review of Supercapacitors: Materials and Devices. *J. Energy Storage* **2019**, *21*, 801–825.
- (52) Xu, H.; Shi, L.; Wang, Z.; Liu, J.; Zhu, J.; Zhao, Y.; Zhang, M.; Yuan, S. Fluorine-Doped Tin Oxide Nanocrystal/Reduced Graphene Oxide Composites as Lithium Ion Battery Anode Material with High Capacity and Cycling Stability. *ACS Appl. Mater. Interfaces* **2015**, *7*, 27486–27493.
- (53) Zhu, X.; Wang, Y.; Shang, K.; He, W.; Ai, X.; Yang, H.; Cao, Y. Improved Rate Capability of the Conducting Functionalized FTO-Coated Li-[Li<sub>0.2</sub>Mn<sub>0.54</sub>Ni<sub>0.13</sub>Co<sub>0.13</sub>] O<sub>2</sub> Cathode Material for Li-Ion Batteries. *J. Mater. Chem. A* **2015**, *3*, 17113–17119.
- (54) Juodkazytė, J.; Šebeka, B.; Savickaja, I.; Petrulevičienė, M.; Butkutė, S.; Jasulaitienė, V.; Selskis, A.; Ramanauskas, R. Electrolytic Splitting of Saline Water: Durable Nickel Oxide Anode for Selective Oxygen Evolution. *Int. J. Hydrogen Energy* **2019**, *44*, 5929–5939.
- (55) Wang, Y.; Marquard, S. L.; Wang, D.; Dares, C.; Meyer, T. J. Single-Site, Heterogeneous Electrochemical Reduction of CO<sub>2</sub> in Water as the Solvent. *ACS Energy Lett.* **2017**, *2*, 1395–1399.
- (56) Nishshanke, G. B. M. M. M.; Thilakarathna, B. D. K. K.; Albinsson, I.; Mellander, B.; Bandara, T. M. W. J. Multi-Layers of TiO<sub>2</sub> Nanoparticles in the Photoelectrode and Binary Iodides in the Gel Polymer Electrolyte Based on Poly (Ethylene Oxide) to Improve Quasi Solid-State Dye-Sensitized Solar Cells. *J. Solid State Electrochem.* **2021**, *25*, 707–720.
- (57) Garcia-Torregrosa, I.; Wijten, J. H. J.; Zanon, S.; Oropeza, F. E.; Hofmann, J. P.; Hensen, E. J. M.; Weckhuysen, B. M. Template-Free Nanostructured Fluorine-Doped Tin Oxide Scaffolds for Photoelectrochemical Water Splitting. *ACS Appl. Mater. Interfaces* **2019**, *11*, 36485–36496.
- (58) Zhao, G.; Xuan, J.; Gong, Q.; Wang, L.; Ren, J.; Sun, M.; Jia, F.; Yin, G.; Liu, B. In Situ Growing Double-Layer TiO<sub>2</sub> Nanorod Arrays on New-Type FTO Electrodes for Low-Concentration NH<sub>3</sub> Detection at Room Temperature. *ACS Appl. Mater. Interfaces* **2020**, *12*, 8573–8582.
- (59) Rahayi, M.; Ehsani, M. H.; Nkele, A. C.; Shahidi, M. M.; Ezema, F. I. Synthesis and Characterization of Tin (IV) Oxide Thin Films. *Opt. Quantum Electron.* **2021**, *53*, No. 222.
- (60) Klug, H. P.; Alexander, L. E. *X-Ray Diffraction Procedures: For Polycrystalline and Amorphous Materials*; Wiley-Interscience: New York, 1974.
- (61) Scherrer, P. J. N. G. W. G. Estimation of the Size and Internal Structure of Colloidal Particles by Means of Röntgen. *Nachr. Ges. Wiss. Göttingen* **1918**, *2*, 96–100.
- (62) Saadiah, M. A.; Zhang, D.; Nagao, Y.; Muzakir, S. K.; Samsudin, A. S. Reducing Crystallinity on Thin Film Based CMC/PVA Hybrid Polymer for Application as a Host in Polymer Electrolytes. *J. Non-Cryst. Solids* **2019**, *511*, 201–211.
- (63) Jackson, N.; Stam, F.; O'Brien, J.; Kailas, L.; Mathewson, A.; O'Murchu, C. Crystallinity and Mechanical Effects from Annealing Parylene Thin Films. *Thin Solid Films* **2016**, *603*, 371–376.
- (64) Dahshan, A.; Aly, K. A. Determination of the Thickness and Optical Constants of Amorphous Ge-Se-Bi Thin Films. *Philos. Mag.* **2009**, *89*, 1005–1016.
- (65) Bandara, T. M. W. J.; Jayasundara, W. J. M. J. S. R.; Fernando, H. D. N. S.; Dissanayake, M. A. K. L.; De Silva, L. A. A.; Fernando, P. S. L.; Furlani, M.; Mellander, B. E. Efficiency Enhancement of Dye-Sensitized Solar Cells with PAN:CsI:LiI Quasi-Solid State (Gel) Electrolytes. *J. Appl. Electrochem.* **2014**, *44*, 917–926.
- (66) Bandara, T. M. W. J.; Mellander, B. E.; Albinsson, I.; Dissanayake, M. A. K. L. Effect of Thermal History and Characterization of Plasticized, Composite Polymer Electrolyte Based on PEO and Tetrapropylammonium Iodide Salt (Pr4N+I-). *Solid State Ionics* **2009**, *180*, 362–367.
- (67) Teo, L. P.; Buraidah, M. H.; Arof, A. K. Polyacrylonitrile-Based Gel Polymer Electrolytes for Dye-Sensitized Solar Cells: A Review. *Ionics* **2020**, *26*, 4215–4238.
- (68) Haacke, G. New Figure of Merit for Transparent Conductors. *J. Appl. Phys.* **1976**, *47*, 4086–4089.
- (69) Rakhshani, A. E.; Makdisi, Y.; Ramazaniyan, H. A. Electronic and Optical Properties of Fluorine-Doped Tin Oxide Films. *J. Appl. Phys.* **1998**, *83*, 1049–1057.

(70) Jun, H. K.; Careem, M. A.; Arof, A. K. Plasmonic Effects of Quantum Size Gold Nanoparticles on Dye-Sensitized Solar Cell. *Mater. Today Proc.* **2016**, *3*, S73–S79.

(71) Kumar, D.; Parmar, K. P. S.; Kuchhal, P. Analysis of Charge Transport Properties of Dye-Sensitized Solar Cell (DSSC) with TiO<sub>2</sub> Working Electrode by Employing Electrochemical Impedance Spectroscopy (EIS). *Int. J. Renewable Energy Res.* **2021**, *11*, 211–222.

(72) Han, L.; Koide, N.; Chiba, Y.; Islam, A.; Mitate, T. Modeling of an Equivalent Circuit for Dye-Sensitized Solar Cells: Improvement of Efficiency of Dye-Sensitized Solar Cells by Reducing Internal Resistance. *Comptes Rendus Chim.* **2006**, *9*, 645–651.